Soft Matter

PAPER

View Article Online
View Journal

Cite this: DOI: 10.1039/c5sm00183h

FRET evidence for untwisting of amyloid fibrils on the surface of model membranes

Galyna Gorbenko,*[a] Valeriya Trusova,[a] Mykhailo Girych,[a] Emi Adachi,[b] Chiharu Mizuguchi,[b] Kenichi Akaji[c] and Hiroyuki Saito[b]

Received 22nd January 2015,
Accepted 26th June 2015

DOI: 10.1039/c5sm00183h

www.rsc.org/softmatter

Apolipoprotein A-I (apoA-I) is an amyloid-forming protein whose amyloidogenic properties are attributed mainly to its N-terminal fragment. Cell membranes are thought to be the primary target for the toxic amyloid aggregates. In the present study Förster resonance energy transfer (FRET) between the membrane fluorescent probe Laurdan as a donor and amyloid-specific dye Thioflavin T (ThT) as an acceptor was employed to explore the interactions of amyloid fibrils from apoA-I variants 1–83/G26R and 1–83/G26R/W@8 with the model membranes composed of phosphatidylcholine and its mixture with cholesterol. The changes in FRET efficiency upon fibril–lipid binding were found to correlate with the extent of protein fibrillization. AFM imaging revealed the presence of two polymorphic states of fibrillar 1–83/G26R/W@8 with the helical and twisted ribbon morphologies. The simulation-based analysis of the experimental FRET profiles provided the arguments in favor of untwisting of fibrillar assemblies upon their interaction with the model membranes. Evidence for the face-on orientation and superficial bilayer location of the membrane-bound fragments of 1–83/G26R/W@8 fibrils was obtained.

Introduction

Amyloid fibrils are self-assembled protein nanostructures distinguished by the core supramolecular β-sheets propagating along the main axis of the fibril with β-strands running perpendicular to this axis.[1] During the past decade this unique type of protein aggregate has been the focus of extensive studies in a broad range of research fields covering molecular biology, biomedicine, design of functional nanomaterials, food science and drug delivery.[2,3] Particular attention has been devoted to identifying the molecular determinants responsible for the involvement of amyloid fibrils and their precursors in a variety of pathological conditions, including neurological diseases, type II diabetes, spongiform encephalopathies, systemic amyloidosis, *etc.*[4,5] Toxic action of amyloid assemblies, which are prone to accumulation both in intracellular and extracellular space, is thought to be primarily targeted at cell membranes.[6,7] Prevailing concepts of amyloid pathogenicity consider the early oligomeric intermediates as the most toxic species whose high membrane-damaging potential arises from the presence of extensive hydrophobic surfaces and high structural flexibility.[8–10] Prefibrillar oligomers have been reported to produce membrane disintegration,[11,12] formation of non-specific ionic channels,[13] uptake of membrane lipids,[14,15] *etc.* However, growing evidence indicates that cytotoxicity is a property characteristic of a continuum of cross-β-sheet-rich structures including mature fibrils. To exemplify, mature lysozyme fibrils displayed the ability to induce mitochondrial failure, increase of plasma membrane permeability,[16] erythrocyte hemolysis and aggregation,[12] *etc.* Furthermore, toxic potential of amyloid assemblies has been hypothesized to correlate with their morphology.[17] Polymorphic behavior seems to be a fundamental feature of the fibrillar state, since morphological variations have been revealed for amyloid fibrils from a range of proteins, including Aβ-peptide,[18] prion protein,[19] α-synuclein,[20] bovine serum albumin,[21] insulin,[22] β-lactoglobulin,[23] *etc.* Amyloid polymorphism can manifest itself at the levels of both protofilament substructures and assembly patterns.[24]

Unique molecular architecture of fibrillar aggregates is maintained by the main-chain hydrogen bonding, ionic pairing, van der Waals, aromatic π–π interactions and hydrogen bonds between amino-acid side chains.[25–27] Amyloid growth is currently regarded as a sequence-specific process, in which certain segments with alternating hydrophobic–hydrophilic amino acid residues, so called ''hot spots'', ensure steric zippering of two β-sheets through van der Waals interactions and entropic free energy gain arising from the release of structured water molecules in the tightly packed fibril core.[28,29]

Protofilament substructural polymorphism arises from the differences in the registration of the β-strands within one

[a] Department of Nuclear and Medical Physics, V.N. Karazin Kharkiv National University, 4 Svobody Sq., Kharkov, 61022, Ukraine. E-mail: galyagor@yahoo.com
[b] Institute of Health Biosciences, Graduate School of Pharmaceutical Sciences, The University of Tokushima, 1-78-1 Shomachi, Tokushima 770-8505, Japan
[c] Department of Medicinal Chemistry, Kyoto Pharmaceutical University, Yamashina-ku, Kyoto 607-8412, Japan

β-sheet; inter-sheet packing and sequence fragments involved in the formation of fibril cores, while assembly polymorphism is determined by the variations in the number of protofilament strands, the character of their packing, degree of twisting, handedness, *etc.*[30] At the mature fibril level, the polymorphic states may be represented by the topologically different structures, such as twisted ribbons, helical ribbons and nanotubes, as has been demonstrated, in particular, for lysozyme,[31] β-lactoglobulin,[23] Aβ-peptide,[32] and bovine serum albumin.[21] The factors underlying the propensity of amyloid fibrils to twist have been supposed to include chirality,[33,34] electrostatic interactions,[35,36] entropic contributions resulting from side chain arrangement, solvent reorganization and backbone dynamics.[35]

The aforesaid existence of correlation between the toxicity of amyloid fibrils and their morphology implies that interactions of fibrillar assemblies with cellular components, especially plasma membranes, are essentially controlled by the supramolecular structure of these aggregates. Furthermore, it might be expected that membrane binding alters the morphological features of fibrillar states, thereby modulating their cytotoxicity. To address this issue, in the present work we explored the lipid bilayer interactions of amyloid fibrils from the N-terminal fragment (1–83) of apolipoprotein A-I (apoA-I). apoA-I is the principal protein component of high-density lipoproteins evoking the efflux of phospholipid and cholesterol from the plasma membrane.[37] Specific variants of human apoA-I, particularly those possessing G26R substitution mutation, have been reported to form amyloid fibrils implicated in renal and liver failure,[38] with the N-terminal fragment being the predominant form of apoA-I in fibrillar deposits.[39,40] Our previous study revealed that the fibrillization of 1–83/G26R/W@8 yields the structures with helical and twisted ribbon morphologies.[41] Analysis of the Förster resonance energy transfer between tryptophan as a donor and amyloid specific dye Thioflavin T as an acceptor allowed us to identify the most probable locations of ThT binding sites within the fibril structure. This provides a basis for the use of 1–83/G26R/W@8 apoA-I mutant as a model protein for ascertaining the effect of fibril–lipid interactions on the morphological characteristics of fibrillar aggregates. For this purpose, in the present study we measured the FRET efficiency between the membrane fluorescent probe Laurdan as a donor and ThT as an acceptor.

Experimental section

Preparation of amyloid fibrils

The N-terminal 1–83 fragment of human apoA-I 1–83, 1–83/G26R and its single tryptophan variant 1–83/G26R/W@8 was expressed and purified as described elsewhere.[42] The apoA-I preparations were at least 95% pure as assessed by SDS-PAGE.

In all experiments, apoA-I variants were freshly dialyzed from 6 M guanidine hydrochloride solution into 10 mM Tris buffer (150 mM NaCl, 0.01% NaN_3, pH 7.4) before use. The reaction of apoA-I fibrillization was carried out at 37 °C in the above buffer. The amyloid nature of fibrillar aggregates was confirmed using the ThT assay.[43] While monitoring the kinetics of fibril growth the protein aliquots (20 μl) were withdrawn at different moments of time from the stock solution (100 μM) undergoing continuous shaking on an orbital rotator. These aliquots were added to 2.2 ml of ThT solution (6.9 μM) before fluorescence measurements.

Preparation of lipid vesicles

Egg yolk phosphatidylcholine (PC) and cholesterol (Chol) were purchased from Avanti Polar Lipids (Alabaster, AL). Laurdan (6-lauroyl-2-dimethylaminonaphthalene) was from Invitrogen Molecular Probes (Eugene, OR, USA).

Large unilamellar vesicles were prepared from PC and PC/Chol (30 mol% Chol) mixtures using an extrusion technique. The thin lipid film was obtained by the evaporation of lipid ethanol solutions and then hydrated with 1.2 ml of 10 mM Tris buffer, 150 mM NaCl, and 0.01% NaN_3 to yield a final lipid concentration of 5 mM. Subsequently, lipid suspension was extruded through a 50 nm pore size polycarbonate filter.

Fluorescence measurements

Fluorescence measurements were performed at 25 °C using a LS-55 spectrofluorimeter equipped with a magnetically stirred cuvette holder (Perkin-Elmer Ltd., Beaconsfield, UK) using 10 mm path-length quartz cuvettes. Emission spectra of Laurdan were recorded with 364 nm excitation wavelength. Excitation and emission slit widths were set at 5 nm.

10 μl of Laurdan solution in ethanol (700 μM) was added to 200 μl of PC or PC/Chol liposomes (1 mM) and incubated for 30 min at 37 °C under stirring. Then the probe–liposome mixtures prepared in such a way were diluted by adding 12 ml of buffer, and 2 ml-portions of the resulting solutions were incubated for 1 hour at 37 °C on an orbital shaker with 40 μl of the examined apoA-I variants (100 μM) being withdrawn at the 20th day of fibrillization reaction, *i.e.* after the completion of fibril growth. Afterwards, 1.6 ml of these samples was placed into a fluorimetric cuvette, diluted with 0.4 ml of buffer and then titrated with ThT.

Fluorescence intensity measured in the presence of ThT at the maximum of the short-wavelength spectral component of Laurdan (440 nm) was corrected for reabsorption and inner filter effects using the following coefficients:[44]

$$k = \frac{\left(1 - 10^{-A_o^{ex}}\right)\left(A_o^{ex} + A_a^{ex}\right)\left(1 - 10^{-A_o^{em}}\right)\left(A_o^{em} + A_a^{em}\right)}{\left(1 - 10^{-(A_o^{ex}+A_a^{ex})}\right)A_o^{ex} \quad \left(1 - 10^{-(A_o^{em}+A_a^{em})}\right)A_o^{em}} \qquad (1)$$

where A_o^{ex} and A_o^{em} are the donor optical densities at the excitation and emission wavelengths in the absence of the acceptor, and A_a^{ex} and A_a^{em} are the acceptor optical densities at the excitation and emission wavelengths, respectively. The efficiency of energy transfer was determined by measuring the decrease of Laurdan fluorescence at 440 nm upon varying the concentration of ThT:

$$E = 1 - \frac{I_{DA}}{I_D} \qquad (2)$$

where I_D and I_{DA} are the donor fluorescence intensities in the absence and the presence of the acceptor, respectively.

Steady-state fluorescence anisotropy of Laurdan was measured at excitation and emission wavelengths of 364 and 440 nm, respectively, with excitation and emission band passes set at 10 nm. The critical distance of energy transfer was calculated as:[45]

$$R_0 = 979(\kappa^2 n_r^{-4} Q_D J)^{1/6}, \quad J = \int_0^\infty F_D(\lambda)\varepsilon_A(\lambda)\lambda^4 \, d\lambda / \int_0^\infty F_D(\lambda) d\lambda \tag{3}$$

where J is the overlap integral derived from numerical integration, $F_D(\lambda)$ is the donor fluorescence intensity, $\varepsilon_A(\lambda)$ is the acceptor molar absorbance at the wavelength λ, n_r is the refractive index of the medium (n_r = 1.4), Q_D is the donor quantum yield, and κ^2 is an orientation factor. The quantum yield of Laurdan was determined using quinine sulphate (Q = 0.58) as a standard. Assuming random reorientation of the donor emission and acceptor absorption transition moments during the emission lifetime (κ^2 = 0.67), the R_0 value was estimated to be 2.9 nm for the Laurdan–ThT donor–acceptor pair (with Q_D = 0.094 for Laurdan).

Atomic force microscopy

The measurement by AFM was carried out using a NanoScope IIIa scanning probe work station equipped with a MultiMode head using an E-series piezoceramic scanner (Digital Instruments, Santa Barbara, CA, USA). AFM probes were single-crystal silicon micro-cantilevers with 300 kHz resonant frequencies and a 26 N m^{-1} spring constant model OMCL-AC160TS-R3 (Olympus, Tokyo, Japan). 10 μl of each sample solution was spotted on freshly cleaved mica (The Nilaco Co., Tokyo, Japan). After washing the mica with distilled water (20 μl), samples were imaged under ambient conditions at room temperature at a scan rate of 0.5 Hz in tapping mode.

Monte Carlo simulation

The FRET profiles obtained for the Laurdan–ThT donor–acceptor pair in the absence of proteins were treated using the Monte-Carlo approach allowing for the distance dependence of the orientation factor in two-dimensional systems.[46] The membrane-associated donors and acceptors were regarded as being confined to the planes separated by a certain distance d_a. The positions of donors and acceptors were generated randomly in a square cell assuming periodic boundary conditions to avoid edge effects. The relative quantum yield (Q_r) of the donor was calculated from the fluorophore coordinates as:

$$Q_r = \frac{I_{DA}}{I_D} = \frac{1}{N_{DL}} \sum_{j=1}^{N_{DL}} \left[1 + \sum_{i=1}^{N_{AL}} \left(\frac{R_o^r \kappa^2 (r_{ij})}{r_{ij}} \right)^6 \right]^{-1} \tag{4}$$

where I_D and I_{DA} are the donor fluorescence intensities in the absence and the presence of the acceptor; r_{ij} is the distance between the jth donor and the ith acceptor; N_{DL} and N_{AL} stand for the number of donors and acceptors in the cell given by:

$$N_{DL} = B_{DL} S_c / L_a S_L; \quad N_{AL} = B_{AL} S_c / L_a S_L \tag{5}$$

where S_c is the cell square; L_a is the concentration of accessible lipids related to the total lipid concentration (L) as L_a = 0.5 L; S_L is the mean area per lipid molecule taken here as 0.65 nm^2 for the PC bilayer and 0.47 nm^2 for the PC/Chol bilayer,[47] and B_{DL} and B_{AL} are the molar concentrations of the membrane-bound Laurdan and ThT, respectively; R_o^r is the part of Förster radius independent of the orientation factor, $R_o^r = 979(n_r^{-4} Q_D J)^{1/6}$. When the donor emission and acceptor absorption transition moments are symmetrically distributed within the cones about certain axes D_x and A_x, the distance-dependent orientation factor is given by:[48]

$$\kappa^2(R) = d_D d_A \left(3\left(\frac{d_a}{R}\right)^2 - 1 \right) + \frac{1 - d_D}{3} + \frac{1 - d_A}{3} + \left(\frac{d_a}{R}\right)^2 (d_D - 2 d_D d_A + d_A) \tag{6}$$

$$d_{D,A} = \left\langle d_{D,A}^x \right\rangle \left(\frac{3}{2} \cos^2 \alpha_{D,A} - \frac{1}{2} \right)$$
$$\left\langle d_{D,A}^x \right\rangle = \left(\frac{3}{2} \cos^2 \psi_{D,A} - \frac{1}{2} \right) \tag{7}$$

where $\psi_{D,A}$ are the cone half-angles and $\alpha_{D,A}$ are the angles made by D_x and A_x with the bilayer normal N. The axial depolarization factors $\langle d_D^x \rangle$ and $\langle d_A^x \rangle$ are related to the experimentally measurable steady-state (r) and fundamental (r_0) anisotropies of the donor and the acceptor:[48]

$$d_{D,A}^x = \pm (r_{D,A} / r_{0D,A})^{1/2} \tag{8}$$

The simulation procedure was repeated for at least 1000 fluorophore configurations until the standard deviation in the E value was less than 2%. The simulation program was scripted using Mathcad 2001 Professional.

Results and discussion

Effect of apoA-I variants on the efficiency of energy transfer between Laurdan and ThT

Fig. 1 shows fibrillization kinetics for three variants of the apoA-I N-terminal fragment, one of which is wild-type 1–83, while the other two possess amyloidogenic substitution mutation G26R. As expected, a characteristic exponential increase in ThT fluorescence was observed only for 1–83/G26R and its single-Trp counterpart 1–83/G26R/W@8, where two Trp residues (Trp50 and Trp72) are substituted for Phe. The drastic increase of ThT fluorescence upon fibril binding results from restricted torsional oscillations of the benzothiazole and aminobenzoyl rings and nearly planar conformation of the dye molecule incorporated in the solvent-exposed grooves spanning across consecutive β-strands parallel to the fibril axis.[49–51] The alignment of ThT molecules along the fibril grooves implies that the spatial distribution of this dye would reproduce the topology of the fibril surface. This led us to the idea to recruit ThT as an energy acceptor in the FRET experiments, since the efficiency of energy transfer essentially depends on spatial arrangement of

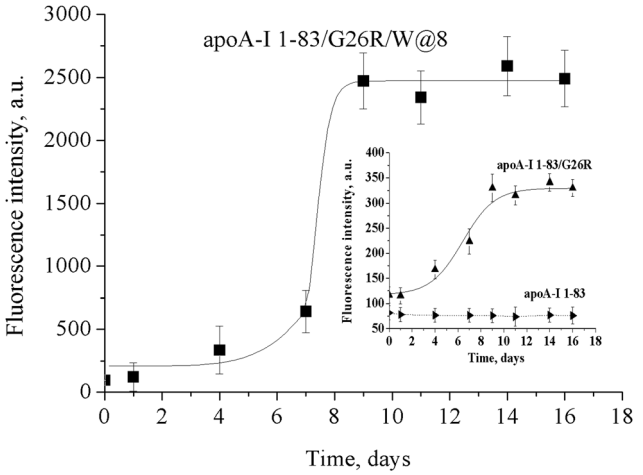

Fig. 1 Fibrillization kinetics of apoA-I variants monitored by measuring ThT fluorescence intensity at 484 nm. The protein concentration was 0.9 μM and the ThT concentration was 6.9 μM.

acceptor molecules around a given donor. Thus, it might be anticipated that analysis of FRET between the donors confined to the lipid bilayer and ThT associated with β-sheet grooves would provide information not only on the lipid binding of amyloid fibrils, but also on the changes in their morphology on the membrane surface. One of the most appropriate energy donors for ThT is a well-characterized fluorescent probe Laurdan. Due to its amphiphilic nature, in the lipid bilayer this dye tends to reside at the polar/nonpolar boundary with the lauric acid tail being anchored in the acyl chain region. Fig. 2 illustrates the changes in Laurdan fluorescence spectra, recorded in PC or PC/Chol model membranes in the absence and the presence of apoA-I variants. The progressive decrease of the probe fluorescence intensity observed upon increasing ThT concentration is indicative of the energy transfer in the donor–acceptor pair Laurdan–ThT. An important feature of Laurdan is its bimodal membrane distribution that manifests itself in the presence of two distinct spectral components, which are attributed to solvent unrelaxed (shorter-wavelength band centered at *ca.* 440 nm) and solvent-relaxed states (longer-wavelength band centered at *ca.* 490 nm).[52,53] To obtain FRET profiles for the examined lipid and lipid–protein systems, we monitored the changes in Laurdan fluorescence intensity at 440 nm, *i.e.* at emission maximum of the short-wavelength component corresponding to the deeper-located probe molecules whose fluorophore moieties reside at the level of the glycerol backbone.[54] As shown in Fig. 3, in PC and PC + 1–83 systems FRET curves are virtually identical, while in the presence of 1–83/G26R and 1–83/G26R/W@8 energy transfer becomes more efficient. Furthermore, FRET efficiency appeared to correlate with the extent of fibrillization that increases in the row 1–83, 1–83/G26R, and 1–83/G26R/W@8. The occurrence of FRET in the absence of proteins indicates that ThT is capable of partitioning into PC bilayers. When ThT is added to PC liposomes with pre-adsorbed apoA-I variants, the dye is distributed between the protein and lipid binding sites. In the membrane systems FRET efficiency depends on the number of acceptor molecules per unit area and the randomness of acceptor distribution over the surface of the lipid bilayer. Obviously, in the case of non-fibrillizing polypeptide 1–83, which does not possess specific binding sites for ThT, the amount of membrane-bound acceptors and their arrangement relative to the donor plane are similar to those in the protein-free PC membranes, as judged from the coinciding FRET curves for PC and PC + 1–83 systems. It is also noteworthy that, according to our observations, the binding of monomeric and oligomeric proteins to lipid vesicles did not affect the FRET between Laurdan and ThT. Since the dye was added after the pre-incubation of apoA-I mutants with liposomes, surface-bound ThT would occupy both protein and lipid binding sites. However, the randomness of ThT distribution and its surface density are supposedly not influenced by the protein monomers and oligomers uniformly distributed over the membrane area. In contrast, adsorption of fibril-forming apoA-I mutants on the surface of lipid vesicles seems to alter spatial density and configuration of membrane-associated ThT molecules, thereby enhancing energy transfer due to the non-random distribution of the protein-bound acceptors. The increase of FRET efficiency in the presence of 1–83/G26R and 1–83/G26R/W@8 suggests that fibril binding to PC liposomes leads to the increase in the number of acceptors within the distance of energy transfer (about two Förster radii from the donor). Since in the case of the non-amyloidogenic apoA-I variant, 1–83, energy transfer between Laurdan and ThT is indistinguishable from that in the protein-free PC liposomes, it can be concluded that FRET enhancement in the presence of 1–83/G26R and 1–83/G26R/W@8 is produced exclusively by fibril-bound ThT molecules.

Polymorphic behavior of 1–83/G26R/W@8 fibrils

Next, allowing for the sensitivity of energy transfer to acceptor spatial distribution, it seemed reasonable to assess whether FRET measurements can be employed for monitoring the changes in fibril morphology. In an attempt to answer this question, we performed simulation-based analysis of the FRET data obtained for 1–83/G26R/W@8, an apoA-I variant with the most pronounced increase of ThT fluorescence, *i.e.* with the highest degree of fibrillization. AFM measurements showed that 1–83/G26R/W@8 fibrils have smooth or twisted appearance indicative of the presence of at least two distinct polymorphs (Fig. 4). The height profiles over the contour length of these polymorphs appeared to be consistent with the twisted ribbon (TR) and helical ribbon (HR) morphologies.[55] To gain more detailed information on the periodicity and morphology of the 1–83/G26R/W@8 fibrils we performed 2D fast Fourier transform (FFT) analysis of the AFM images using Gwyddion software. As shown in Fig. 5 and 6, the FFT intensity profiles of both twisted and helical ribbons have strong peaks in the area related to average pitch size, being indicative of the substantial periodicity of the corresponding amyloid structures. The fact that in the case of helical ribbon fibrils such periodicity is most pronounced only in the regions of fibril bending and could not be detected by the height profile analysis which may indicate

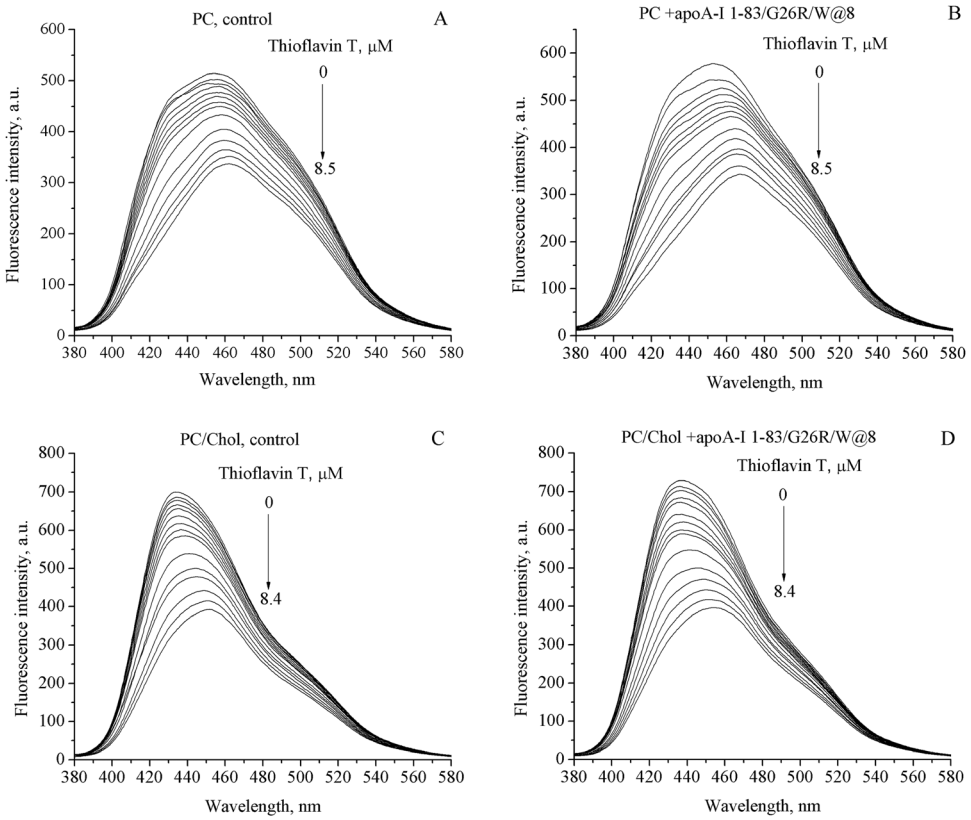

Fig. 2 Emission spectra of Laurdan recorded upon varying ThT concentration in the lipid and lipid–protein systems. (A) PC, control; (B) PC + fibrillar 1–83/G26R/W@8; (C) PC/Chol (30 mol% Chol), control; (D) PC/Chol + fibrillar 1–83/G26R/W@8. The lipid concentration was 13 μM, the protein concentration was 1.6 μM, and the Laurdan concentration was 0.5 μM.

that the gap between edges of the helical ribbon filaments is too small to be distinguished with the tip of 7 nm radius. This assumption is corroborated by the observed average width of the filaments (~10 nm) and the pitch size of helical ribbon (~16 nm), which yields an approximate gap size of about 6 nm. It should also be noted in this context that helical ribbon-like fibril depicted in Fig. 4 as "profile 1" is the result of misplacement because it has an invariant height profile along its whole length and this type of fibril represents the predominant population of polymorphs in the AFM images.

Heterogeneity of ThT binding sites on 1–83/G26R/W@8 fibrils

Structural polymorphism of 1–83/G26R/W@8 fibrils manifests itself in the heterogeneity of ThT binding sites. This issue was addressed in our previous study where the method of double fluorimetric titration was employed to determine quantitative characteristics of ThT interaction with 1–83/G26R/W@8 fibrils (association constant, K_a, and binding stoichiometry, n, in moles of ThT per mole of protein monomers).[41] The observed concave-up appearance of ThT-fibril binding data presented in Scatchard coordinates was interpreted as arising from the existence of two types of ThT binding sites pertaining to TR and HR polymorphs, respectively. The global fitting of two-dimensional data arrays obtained upon varying concentrations of both ThT and protein yielded the following sets of binding parameters: $K_{a1} = (6.2 \pm 0.7)\ \mu M^{-1}$, $n_1 = 0.1 \pm 0.02$ (high-affinity centers); $K_{a2} = (0.14 \pm 0.03)\ \mu M^{-1}$, $n_2 = 0.17 \pm 0.03$, (low-affinity centers). Based on the β-strand–loop–β-strand structural model of 1–83/G26R/W@8 fibrils and analysis of FRET between Trp8 and ThT, we supposed that high-affinity ThT binding sites reside within the groove T16_Y18 on the helical ribbon polymorphs whose constant curvature favors a nearly planar motionally restricted conformation of the dye, while low-affinity sites are lined up at the groove D20_L22 on the twisted ribbon polymorphs with a varying curvature.[41]

Simulation-based analysis of FRET data

The above findings created the prerequisites for quantitative interpretation of the FRET results presented here. The employed strategy of simulation-based data analysis involved the following main steps: (i) quantification of ThT binding to TR, HR fibrillar structures and lipid bilayers; (ii) generation of the donor and acceptor coordinates in a virtual box; (iii) calculation of the energy transfer efficiency for any given spatial configuration of donors and acceptors; (iv) determining what kind of acceptor arrangement relative to the donors is consistent with the experimental FRET profiles. The relative quantum yield averaged over all donors in the box was calculated as:

$$Q_r = \frac{1}{N_D}\sum_{j=1}^{N_D}\left[1+\sum_{i=1}^{N_{AC}}\left(\frac{R_o^r\kappa^2}{r_{ij}}\right)^6\right]^{-1} \quad (9)$$

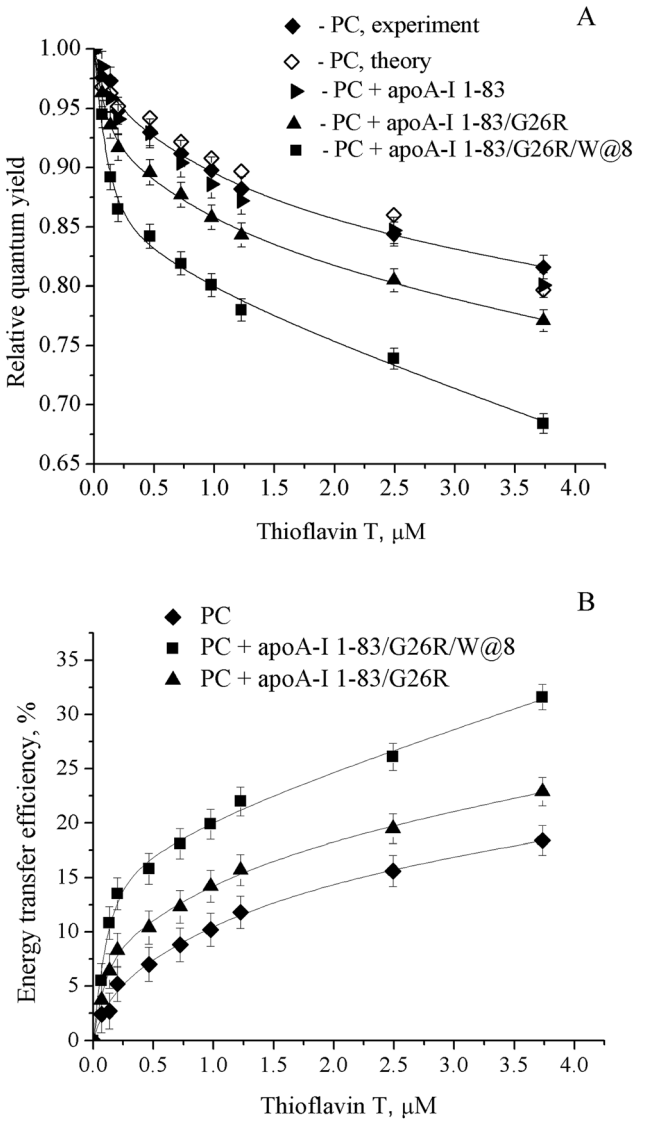

Fig. 3 (A) Relative quantum yield of Laurdan in PC and PC + apoA variant systems as a function of Thioflavin T concentration. The hollow diamonds indicate Q_r values calculated from eqn (4) with $\lg K_P = 2.8$ and $d_a = 0$, the values of optimizing parameters providing the best agreement between the experiment and theory. (B) Efficiency of energy transfer between Laurdan and ThT in PC and PC + apoA variant systems as a function of Thioflavin T concentration. The lipid concentration was 13 μM, the protein concentration was 1.6 μM, and the Laurdan concentration was 0.5 μM.

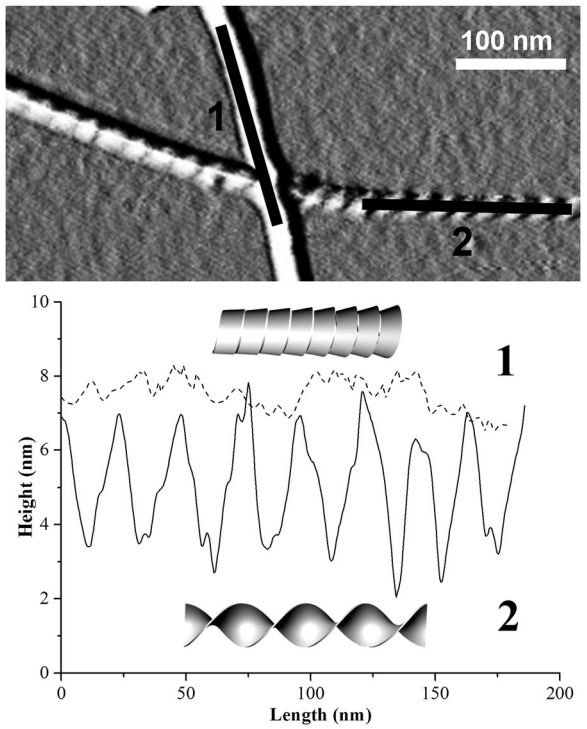

Fig. 4 Atomic force microscopy images of 1–83/G26R/W@8 fibrils illustrating the presence of helical and twisted ribbon polymorphs and height profiles over the contour length obtained for these polymorphs using ImageJ software.

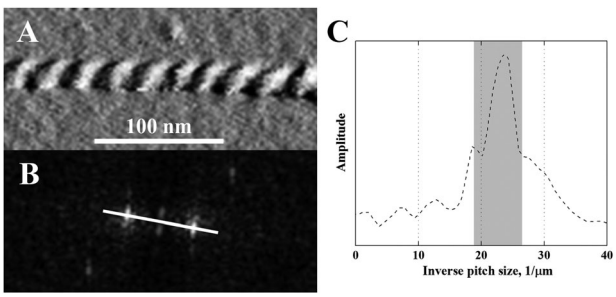

Fig. 5 (A) AFM height image of twisted ribbon-like fibril polymorphs. (B) 2D Fast Fourier transform of the corresponding AFM image. (C) Intensity profile along the white line of the FFT image (due to symmetry only half of the profile is shown). The grey stripe indicates a peak related to the distribution of fibril pitch size.

where N_D and N_{AC} denote the number of donors and acceptors in the box, respectively; l_b is the edge length of the square box taken as $10R_0$. The value of orientation factor was varied between $\kappa_{min}^2 = 2/3(1 - 0.5(d_D + d_A))$ and $\kappa_{max}^2 = 2/3(1 + d_D + d_A + 3d_Dd_A)$ where d_D and d_A were evaluated from the fluorescence anisotropy measurements using eqn (8).[48] The N_{AC} value was estimated as the sum of the amounts of ThT species associated with HR (N_{HR}), TR (N_{TR}) and lipids (N_L). The molar concentrations of these species (B_{HR}, B_{TR}, and B_{AL}, respectively) were calculated for any given total concentration of ThT by solving the system of the following equations:

$$B_{HR} = \frac{n_1 P(Z - B_{HR} - B_{TR} - B_{AL})}{1/K_{a1} + (Z - B_{HR} - B_{TR} - B_{AL})};$$

$$B_{TR} = \frac{n_2 P(Z - B_{HR} - B_{TR} - B_{AL})}{1/K_{a2} + (Z - B_{HR} - B_{TR} - B_{AL})}; \quad (10)$$

$$B_{AL} = \frac{K_P(Z - B_{HR} - B_{TR} - B_{AL})V_L}{V_W + K_P V_L}$$

where P is the total concentration of protein monomers, K_P is the dye partition coefficient characterizing ThT interaction with the lipid bilayer; Z is the total molar concentration of ThT;

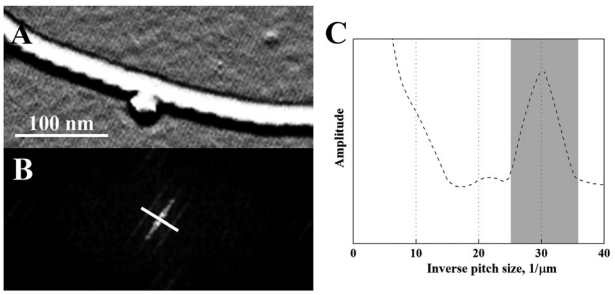

Fig. 6 (A) AFM height image of helical ribbon-like fibril polymorphs. (B) 2D Fast Fourier transform of the corresponding AFM image. (C) Intensity profile along the white line of the FFT image (due to symmetry only half of the profile is shown). The grey stripe indicates a peak related to the distribution of fibril pitch size.

V_L and V_W are the volumes of lipid and aqueous phases, respectively. The K_P value was estimated from the Monte-Carlo analysis of the FRET profiles measured in the absence of protein through minimization of the error function:

$$\chi^2 = \frac{1}{N}\sum_{i=1}^{N}\left(Q_{ri}^{e} - Q_{ri}^{t}\right)^2 \qquad (11)$$

where N is the number of experimental points; Q_r^e is the experimental Q_r value, and Q_r^t is the relative quantum yield calculated from eqn (4)–(8) with B_{AL} being evaluated as follows:

$$B_{AL} = \frac{K_P V_L Z}{V_W + K_P V_L} \qquad (12)$$

As illustrated in Fig. 7, in the case of PC liposomes the error function attains its minimum at $\lg K_P \sim 2.8$ and $d_a \sim 0$, suggesting that Laurdan and ThT fluorophore moieties are planarly distributed at nearly the same level within the lipid bilayer.

Distribution of ThT between protein and lipid binding sites

The foregoing evaluation of the quantitative characteristics of ThT association with the lipid bilayer, as well as HR and TR fibril polymorphs, allowed us to assess how this dye is distributed between the lipid and protein binding sites (Fig. 8). The FRET signal originates from the ThT molecules nonspecifically bound to lipid vesicles and specifically associated with fibrillar protein.

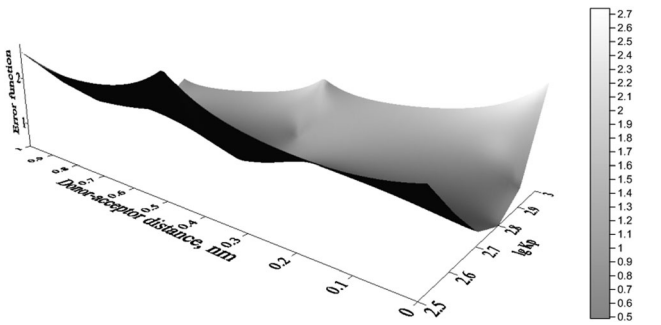

Fig. 7 Error function calculated from eqn (11) while applying the least-square minimization procedure to analyze FRET between Laurdan and ThT in PC liposomes. The Z-axis shows the χ^2 value multiplied by 10^3.

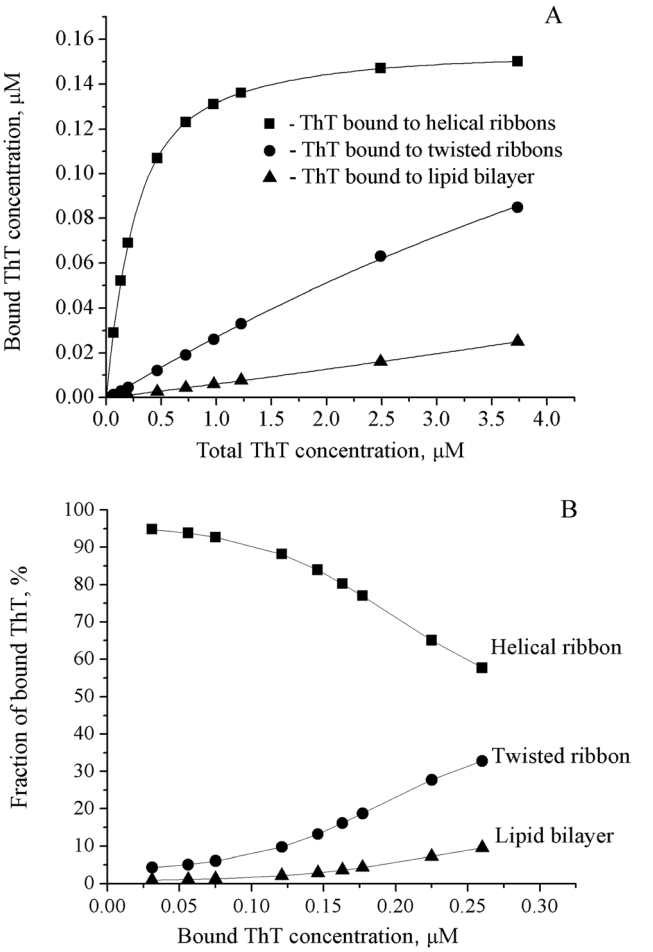

Fig. 8 Distribution of Thioflavin T between the binding sites located in the lipid bilayer and in the surface grooves of 1–83/G26R/W@8 fibrils (high-affinity sites of the helical ribbons and low-affinity sites of the twisted ribbons). (A) Concentration of ThT bound to HR, TR or lipid bilayer as a function of the total ThT concentration. (B) Fractions of ThT associated with protein and lipid binding sites (relative to the total amount of bound ThT).

As shown in Fig. 8B, the fraction of ThT distributed in the lipid phase (relative to the total amount of bound ThT) does not exceed 10%, while the E value reaches ~18% at the maximum ThT concentration analyzed (Fig. 3B). For the PC + 1–83/G26R/W@8 system most of the bound ThT (~90%) reside on the protein sites, accounting for the increase in E value at each titration point, with maximum $E \sim 32\%$. Subsequent determination of the surface density of lipid-bound acceptors and linear density (the number of ThT molecules per protein monomer) of HR- and TR-associated acceptors permitted calculation of the number of various ThT species (N_L, N_{HR} and N_{TR}) in the box.

Assessment of FRET sensitivity to the morphology of membrane-bound fibrils

In the following analysis, several possibilities have been considered. First, fibrils were regarded as retaining their HR or TR morphology when interacting with the lipid vesicles. The donors were treated as being confined to a plane parallel to the membrane surface and located at a certain distance r_{fd} from

the fibril axis (Fig. 9). The lengths of HR (l_{HR}) and TR (l_{TR}) fibrils in the box relative to l_b were defined by the parameters $s_{HR} = l_{HR}/l_b$ and $s_{TR} = l_{TR}/l_b$. Assuming that the fibril axis is directed along the *Y*-axis, the coordinates of ThT molecules distributed over the twisted ribbon structure (X_{A_k}, Y_{A_k}, Z_{A_k}) were defined as:

$$\begin{aligned} X_{A_k} &= (l_b - 0.5w + d_{TR})N_R \\ &\quad + (0.5w - d_{TR})\cos\left(\frac{2\pi d_m n_{TR} k}{P_{TR}}\right); \\ Y_{A_k} &= n_{TR} d_m k; \\ Z_{A_k} &= (0.5w - d_{TR})\sin\left(\frac{2\pi d_m n_{TR} k}{P_{TR}}\right) \end{aligned} \quad (13)$$

where *w*, fibril width; P_{TR}, TR pitch; d_m, the distance between protein monomers (along the *Y*-axis); n_{TR}, the number of protein monomers per acceptor molecule; d_{TR}, the ThT distance from the protofilament edge in the twisted ribbon structure; N_R, a random number chosen from a uniform distribution between 0 and 1. Similar relationships were employed to generate the coordinates of acceptors (X_{A_l}, Y_{A_l}, Z_{A_l}) in the helical ribbon structure:

$$\begin{aligned} X_{A_l} &= (l_b - r_h)N_R + r_h\cos\left(\frac{2\pi d_h n_{HR} l}{P_{HR}}\right); \\ Y_{A_l} &= \frac{d_{HR}}{\cos\psi} + n_{HR} d_h l; \\ Z_{A_l} &= r_{fd} - r_h + r_h\sin\left(\frac{2\pi d_h n_{HR} l}{P_{HR}}\right); \\ P_{HR} &= 2\pi r_h \tan\psi \end{aligned} \quad (14)$$

where r_h, helix radius; P_{HR}, HR pitch; ψ, pitch angle; $d_h = d_m \sin\psi$, the distance between protein monomers along the *Y*-axis, coinciding with the helix axis; n_{HR}, the number of protein monomers per acceptor molecule; d_{HR}, the ThT distance from the protofilament edge in the helical ribbon structure. Using eqn (9)–(14) we simulated Laurdan–ThT FRET for the two types of fibril polymorphs whose structural parameters were derived from the AFM images of 1–83/G26R/W@8 fibrils. The width and the pitch of the twisted ribbon were proved to be $w \sim 10$ nm; $P_{TR} \sim 50$ nm, while the radius and the pitch angle of the helical ribbon were estimated to be $r_h \sim 5$ nm; $\psi \sim 70°$. The value of d_m was taken as 0.47 nm, the interstrand distance in the β-sheet, whereas n_{TR} and n_{HR} were obtained from the above ThT–fibril binding data, $n_{TR} = 11$ and $n_{HR} = 10$. The estimates for d_{TR} and d_{HR} were obtained from the structural model of 1–83/G26R/W@8 fibrils proposed in our recent study.[41] Reasoning from the self-associating properties of the 1–83 apoA-I N-terminal fragment recovered from AGGRESCAN,[56] Zyggregator[57] and TANGO[58] algorithms, as well as available experimental evidence of the β-sheet propensities of apoA-I segments,[59,60] we assumed that superficial grooves which could accommodate ThT molecules are formed by the solvent-exposed residues L14_T16_Y18_D20_L22_D24_R26_D28_V30 in the N-terminal β-sheet layer and by the residues Q41_N43_K45_L47_N49_D51, S52_T54_T56_S58 in the C-terminal β-sheet layer. Subsequent analysis of FRET data acquired for the W8-ThT donor–acceptor pair showed that HR groove T16_Y18 and TR groove D20_L22 are the most likely candidates for ThT binding sites. Taking the propagation of an extended polypeptide chain as ~0.35 nm per residue one obtains that maximum separation between W8 and T16_Y18 grooves is ~3.2 nm, while for D20_L22 this separation is ~4.6 nm. Analogous estimates for L14 which resides at the beginning of the rigid fibril core were proved to be ~1.1 nm and 2.4 nm, respectively. Since W8 is located outside of the β-sheet core, approximately in the middle of the flexible region of the polypeptide chain, it seemed sensible to take ThT distances from L14 and W8 as the lower and upper limits for d_{HR} and d_{TR}, respectively, so that d_{HR} was allowed to vary from 1.1 to 3.2 nm, while d_{TR} – from 2.4 to 4.6 nm.

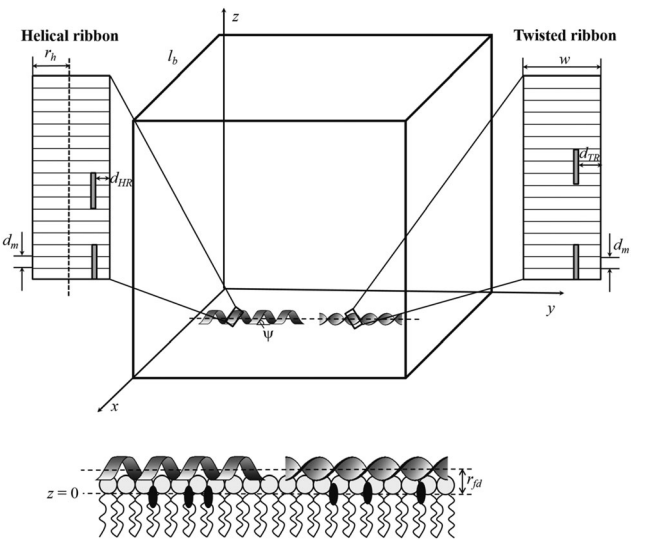

Fig. 9 Schematic representations of the parameters used in the simulation-based analysis of the FRET data. ThT molecules are depicted as grey rectangles, while Laurdan molecules are drawn as black ovals.

This kind of data analysis was aimed at elucidating what set of optimizing parameters $\{r_{fd}, s_{HR}, s_{TR}\}$ provides the best agreement between experimentally measured and theoretically calculated Q_r values. However, on the assumption that membrane-associated fibrils keep their HR or TR structure we did not manage to find any meaningful combination of the above fixed and varied parameters capable of describing the experimental FRET profiles. This led us to suppose that fibrillar 1–83/G26R/W@8 undergoes lipid-induced structural changes involving the untwisting of the helical and twisted ribbons. Indeed, as illustrated in Fig. 10A, the discrepancy between the experiment and theory becomes less pronounced when fibril-bound acceptors are treated as being arranged along the lines parallel to the bilayer surface, in accordance with the view that ThT resides along surface side-chain grooves running parallel to the long fibril axis.[61,62] Furthermore, the best fitting of the FRET profile was achieved in the case when the orientation factor was taken as being dependent on the donor–acceptor distance (Fig. 10A), suggesting that ThT is similar in its orientational behavior to the

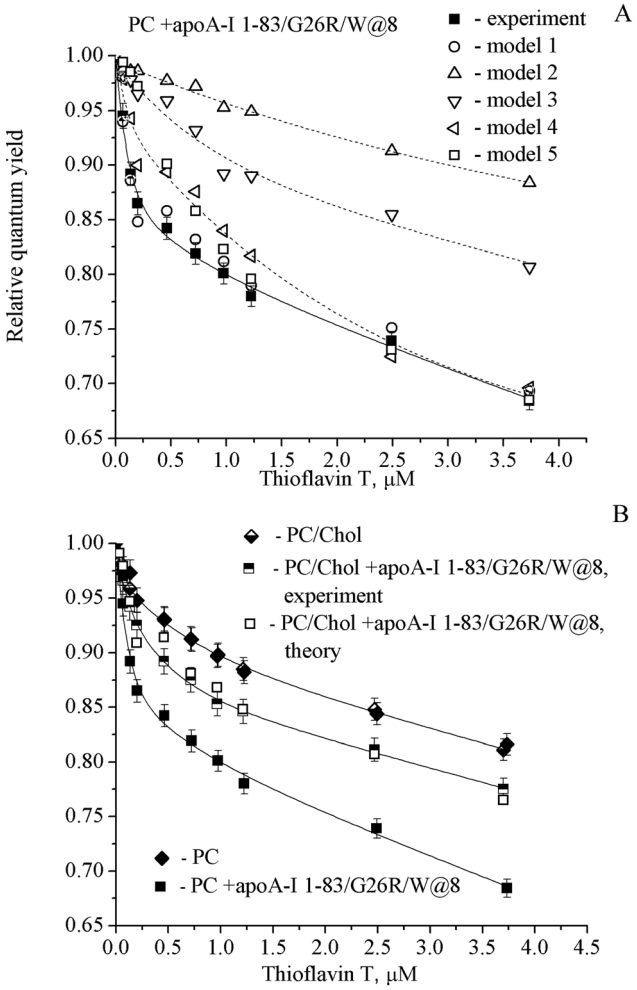

Fig. 10 Relative quantum yield of Laurdan in PC and PC/Chol liposomes measured as a function of Thioflavin T concentration in the absence and the presence of fibrillar 1–83/G26R/W@8. (A) The hollow symbols refer to the Q_r values calculated in terms of the following theoretical models: model 1 – linear arrangement of acceptors, distance-dependent orientation factor, three acceptor populations (ThT bound to untwisted HR, TR and lipid bilayers); model 2 – helical arrangement of acceptors, fixed orientation factor, three acceptor populations (ThT bound to unmodified HR, TR and lipid bilayers); model 3 – linear arrangement of acceptors, fixed orientation factor, three acceptor populations (ThT bound to untwisted HR, TR and lipid bilayers); model 4 – linear arrangement of acceptors, distance-dependent orientation factor, two acceptor populations (ThT bound to undistinguishable sites on untwisted HR or TR, and lipid bilayers); model 5 – helical arrangement of acceptors, distance-dependent orientation factor, four acceptor populations (ThT bound to unmodified HR, TR, bulk lipid bilayers ($\lg K_P$ = 3.8) and linear bilayer defects surrounding HR or TR ($\lg K_P$ = 5.0)). (B) Comparison of FRET profiles acquired for PC and PC/Chol systems. The hollow squares indicate Q_r values calculated in terms of model 1 for the system PC/Chol + fibrillar 1–83/G26R/W@8.

membrane fluorophores.[46] One hypothesis to explain this finding is that the adsorption of a certain fibril fragment on the membrane surface produces structural transformations of superficial fibril grooves arising from the rearrangement of the hydrogen-bond network in a lipid environment. As a consequence, the properties of ThT binding sites become an intermediate between those of the fibrillar structure and the lipid phase, and ThT orientational properties as an energy acceptor for Laurdan resemble those of the membrane-bound dyes.

Evaluating the possibility of fibril untwisting at the lipid–water interface

In the following, it seems of importance to assess some additional possible explanations for the observed effects, alternative to untwisting of the membrane-bound fibrils. First, it can be supposed that there exists a population of flat filaments preferentially associating with the lipid bilayer. However, it seems unlikely that such polymorphs play a determining role in our case since: (i) flat filaments are rather rare structures in the amyloid morphology due to amino acid chirality and intrinsic fibril propensity for twisting; and (ii) taking into account that the height-to-width ratio of flat ribbons in AFM images is at least twice lower than that of twisted/helical ribbons, we failed to find any proof for the presence of flat filaments in our samples. A second alternative explanation of the obtained results involves fibril-induced structural modification of the lipid bilayer coupled with the enhancement of ThT membrane partitioning. Indeed, our recent study revealed that 1–83/G26R/W@8 fibrils bring about the increase of bilayer hydration and reduction of lipid packing density in the interfacial region.[63] In principle, it cannot be excluded that fibril–liposome binding leads to the formation of linear defects in the lipid bilayer in which ThT molecules are arranged in linear rows. To evaluate this possibility, we simulated the situation when the helical arrays of fibril-bound ThT coexist with two types of lipid-bound ThT species: (i) randomly distributed in a bulk and (ii) organized into linear arrays along the fibril length. However, even assuming that fibril binding gives rise not only to the formation of linear defects, but also to the substantial reorganization of the lipid bilayer structure followed by the increase of ThT partitioning, we failed to reproduce the experimental FRET profile (Fig. 10A, model 5). Therefore, we are prone to attribute the observed effects to the membrane-mediated untwisting of 1–83/G26R/W@8 fibrils (Fig. 11).

It appeared that the best agreement between the experimental and simulation results is reached for $l_{HR} \sim 29$ nm and $l_{TR} \sim 6$ nm, ''face-on'' rather than ''edge-on'' orientation of the surface-bound protofilament, and separation of the acceptor

Fig. 11 Schematic illustration for untwisting of the 1–83/G26R/W@8 fibrils on the surface of the lipid bilayer.

linear arrays from the donor plane $d_{HR} \sim 1$ nm and $d_{TR} \sim 1$ nm. Allowing for Laurdan bilayer location at the polar/nonpolar boundary, the obtained estimates for donor–acceptor separation suggest that linear arrays of fibril-bound ThT reside at the lipid–water interface with ThT accommodating grooves facing the aqueous phase. Since the distance between β-sheets in a β-strand–loop–β-strand structure is *ca.* 1 nm, the above values of d_{HR} and d_{TR} are consistent with membrane penetration of β-strands at the depth ~ 1 nm, till the level of initial acyl chain carbons. Next, using the values of l_{HR} and l_{TR} we made an attempt to describe fibril–lipid binding in terms of the number of lipid molecules per protein monomer. Taking the surface area per lipid headgroup as 0.65 nm^2, it follows that the box with an edge length of 29 nm contains 1294 lipid molecules, while the total length of untwisted HR and TR is ~35 nm, corresponding to ~75 protein monomers. Hence, in a planar ribbon configuration of 1–83/G26R/W@8 fibrils associated with PC liposomes the number of lipid molecules per protein monomer is ~17. Analogous estimates for PC/Chol liposomes (Fig. 10B) turned out to be: l_{HR} ~17 nm, $l_{TR} = 0$, $d_{HR} \sim 2$ nm, and the number of lipid molecules per protein monomer ~34, suggesting that in the presence of cholesterol fibril penetration in the polar membrane region is hampered and the fibril–lipid contact area is reduced about twofold.

In the following, to reinforce the above assumption on the orientation of fibrillar 1–83/G26R/W@8 relative to the membrane surface, we employed the HeliQuest online server offering the opportunity to evaluate the mean hydrophobicity ($\langle H \rangle$), hydrophobic moment (μ_H), net charge (z) and eventually lipid discrimination factor D, characterizing lipid binding affinity of a certain polypeptide fragment.[64,65] If ThT accommodating grooves face the aqueous phase, the core sequence Q41–S58 must reside within fibril–membrane contact area. The HeliQuest analysis of the 1–83/G26R/W@8 sequence showed that this peptide possesses four most probable membrane-binding regions, *viz.* R10–R27, K23–K40, L44–R61, and S52–Q69, with the highest lipid-associating potential corresponding to L44–R61, thereby corroborating the conjecture that the β-sheet containing the residues 41–58 faces the membrane surface.

As judged from AFM images, the persistence length of 1–83/G26R/W@8 fibrils is *ca.* 2 μM, indicative of their high structural rigidity. The persistence length is defined as $l_P = -s/2 \ln \langle \cos \theta(s) \rangle$, where θ is the angle between the tangent vectors to the chain at two points separated by a contour distance s. This characteristic is regarded as a measure of the elastic properties of a molecule, since it relates to the Young's modulus of the polymer (Y) and the area moment of inertia of the polymer cross-section (I): $l_P = YI/k_BT$, where k_B is the Boltzmann constant and T is the temperature.[23] The Young's modulus of amyloid fibrils is ~1 GPa, while the lipid bilayer is much more flexible ($Y \sim 1$ MPa).[66] The adsorption of lipid vesicles along the lengthy fibrillar strands may be considered as producing a kind of composite material whose stiffness is given by the volume-weighted average of Young's moduli of its constituents, according to the rule of mixtures.[67] Thus, amyloid fibrils might be expected to stiffen and distort the lipid bilayer. Indeed, membrane distortion has been observed, for instance, for the aggregated Aβ-peptide,[68,69] lysozyme,[70] β_2-microglobulin.[71] On the other hand, membrane interactions of fibrillar structures seem to affect their persistence and rigidity. The results of FRET analysis presented here suggest that helical and twisted ribbon polymorphs of 1–83/G26R/W@8 fibrils experience untwisting upon adsorption on the surface of PC and PC/Chol bilayers. Importantly, our findings are in accordance with a recent theoretical analysis of the conformational behavior of surface-bound polymers with an intrinsic twist and anisotropic bending stiffness.[72] A strong coupling between the twist degrees of freedom of a helical polymer and the strength of surface interactions was demonstrated to result in progressive unwinding of the helical twist with increasing the binding affinity. It was supposed that above a certain critical value of the binding strength, depending on the torsional modulus and the intrinsic twist rate, the polymer can adopt a conformation with a zero twist, surface bound state with a homogeneous stiffness. Taking as an example the electrostatic polymer–surface interactions, the authors concluded that surface charge densities characteristic of cell membranes are sufficient to cause full untwisting of the helical biofilaments like F-actin.[72] In the fibril–lipid systems described here the role of electrostatic interactions is unlikely to be significant because the FRET experiments were conducted with the uncharged liposomes at elevated ionic strength (0.15 M). Hence, the membrane association of 1–83/G26R/W@8 fibrils is most probably driven by van der Waals and hydrophobic interactions whose strength can be comparable or exceed that of electrostatic contacts, thereby providing the conditions for untwisting of the helical and twisted ribbons at the lipid–water interface. To strengthen the above rationales, it should be noted that the fibril periodic pitch is sensitive to environmental factors, particularly, to variations in ionic strength. As was demonstrated by Adamcik and Mezzenga, the increase of the salt content resulted in the gradual untwisting of β-lactoglobulin fibrils.[73] The fine balance between competing electrostatic energy and torsional elastic energy was supposed to control the twisting pitch of amyloid fibrils. Moreover, mild temperature and salinity changes were found to distort the hydrogen bonding network stabilizing the core of apo-α-lactalbumin fibrils, thereby promoting their refolding.[74] These observations, along with other evidence, compromise the concept of the extreme stability of amyloid fibrils.

Conclusions

In summary, the key findings of the present study can be outlined as follows.

(1) Analysis of the Förster energy transfer between the membrane fluorescent probe Laurdan and amyloid-specific dye Thioflavin T indicated that amyloid fibrils from the N-terminal fragment (1–83) of apoA-I are capable of associating with PC and PC/Chol bilayers. Fibril–membrane binding manifests itself in the enhancement of energy transfer in protein–lipid mixtures compared to the neat lipid systems, with the magnitude of this effect being correlated with the degree of fibrillization.

(2) Simulation-based interpretation of the FRET results acquired for fibrillar apoA-I variant 1–83/G26R/W@8 possessing the helical and twisted ribbon morphologies provided evidence for untwisting of the fibril structure in the membrane-bound state. The discrimination between possible spatial arrangements of the donors and acceptors revealed the prevalence of planar ribbon configuration and face-on orientation of the fibril fragments associating with the lipid bilayer.

(3) FRET-based evaluation of the donor–acceptor separation revealed that β-strands of 1–83/G26R/W@8 fibrils insert into the interfacial region of the PC bilayer, with ThT-binding grooves facing the aqueous phase. Cholesterol was found to decrease the extent of fibril–membrane binding and prevent β-strand penetration in the lipid bilayer interior.

Although the biological relevance of these observations remains to be elucidated, there is no doubt that in-depth characterization of the membrane-associating behavior of fibrillar assemblies is critically required for identifying the membrane-related determinants of amyloid cytotoxicity. Furthermore, the possibility of tuning the morphological characteristics of amyloid fibrils by the surfaces may prove of interest in the context of nanotechnological applications of this type of protein aggregate.

Acknowledgements

This work was partly supported by the Grant-in-Aid for Scientific Research 25293006 (to H.S.) from the Japan Society for the Promotion of Science.

References

1 K. E. Marshall and L. C. Serpell, *Open Biol. J.*, 2009, **2**, 185–192.
2 T. P. J. Knowles and M. J. Buehler, *Nat. Nanotechnol.*, 2011, **6**, 469–479.
3 C. A. E. Hauser, S. Maurer-Stroh and I. C. Martins, *Chem. Soc. Rev.*, 2014, **43**, 5326–5345.
4 M. Stefani, *Biochim. Biophys. Acta*, 2004, **1739**, 5–25.
5 F. Chiti and C. M. Dobson, *Annu. Rev. Biochem.*, 2006, **75**, 333–366.
6 M. Bucciantini, S. Rigacci and M. Stefani, *J. Phys. Chem. Lett.*, 2014, **5**, 517–527.
7 S. M. Butterfield and H. A. Lashuel, *Angew. Chem., Int. Ed.*, 2010, **49**, 5628–5654.
8 P. K. J. Kinnunen, *Open Biol. J.*, 2009, **2**, 163–175.
9 A. Relini, O. Cavalleri, R. Rolandi and A. Gliozzi, *Chem. Phys. Lipids*, 2009, **158**, 1–9.
10 M. Stefani, *FEBS J.*, 2010, **277**, 4602–4613.
11 A. A. Meratan, A. Ghasemi and M. Nemat-Gorgani, *J. Mol. Biol.*, 2011, **409**, 826–838.
12 B. Huang, J. He, J. Ren, X. Y. Yan and C. M. Zeng, *Biochemistry*, 2009, **48**, 5794–5800.
13 B. Caughey and P. T. Lansbury, *Annu. Rev. Neurosci.*, 2003, **26**, 267–298.
14 E. Sparr, M. F. M. Engel, D. V. Sakharov, M. Sprong, J. Jacobs, B. de Kruijf, J. W. M. Hoppener and J. A. Killian, *FEBS Lett.*, 2004, **577**, 117–120.
15 M. F. Engel, L. Khemtemourian, C. C. Kleijer, H. J. Meeldijk, J. Jacobs, A. J. Verkleij, B. de Kruijff, J. A. Killian and J. W. Höppener, *Proc. Natl. Acad. Sci. U. S. A.*, 2008, **105**, 6033–6038.
16 A. L. Gharibyan, V. Zamotin, K. Yanamandra, O. S. Moskaleva, B. A. Margulis, I. A. Kostanyan and L. A. Morozova-Roche, *J. Mol. Biol.*, 2007, **365**, 1337–1349.
17 A. T. Petkova, R. D. Leapman, Z. Guo, W. M. Yau, M. P. Mattson and R. Tycko, *Science*, 2005, **307**, 262–265.
18 Y. Miller, B. Ma and R. Nussinov, *Chem. Rev.*, 2010, **110**, 4820–4838.
19 M. Anderson, O. V. Bocharova, N. Makarava, L. Breydo, V. V. Salnikov and I. V. Baskakov, *J. Mol. Biol.*, 2006, **358**, 580–596.
20 H. Heise, W. Hoyer, S. Becker, O. C. Andronesi, D. Riedel and M. Baldus, *Proc. Natl. Acad. Sci. U. S. A.*, 2005, **102**, 15871–15876.
21 I. Usov, J. Adamcik and R. Mezzenga, *ACS Nano*, 2013, **7**, 10465–10474.
22 D. Kurouski, R. K. Dukor, X. Lu, L. A. Nafie and I. K. Lednev, *Chem. Commun.*, 2012, **48**, 2837–2839.
23 J. Adamcik, J. M. Jung, J. Flakowski, P. De Los Rios, G. Dietler and R. Mezzenga, *Nat. Nanotechnol.*, 2010, **5**, 423–428.
24 R. Kodali and R. Wetzel, *Curr. Opin. Struct. Biol.*, 2007, **17**, 48–57.
25 R. Nelson, M. R. Sawaya, M. Balbirnie, A. Madsen, C. Riekel, R. Grothe and D. Eisenberg, *Nature*, 2005, **435**, 773–778.
26 O. S. Makin, E. Atkins, P. Sikorski, J. Johansson and L. C. Serpell, *Proc. Natl. Acad. Sci. U. S. A.*, 2005, **102**, 315–320.
27 A. T. Petkova, W. M. Yau and R. Tycko, *Biochemistry*, 2006, **45**, 498–512.
28 M. R. Sawaya, S. Sambashivan, R. Nelson, M. Ivanova, S. Sievers, M. Apostol, M. Thompson, M. Balbirnie, J. Wiltzius, H. McFarlane, A. Madsen, C. Riekel and D. Eisenberg, *Nature*, 2007, **447**, 453–457.
29 A. D. Williams, S. Shivaprasad and R. Wetzel, *J. Mol. Biol.*, 2006, **357**, 1283–1294.
30 L. R. Volpatti, M. Vendruscolo, C. M. Dobson and T. P. J. Knowles, *ACS Nano*, 2013, **7**, 10443–10448.
31 C. Lara, J. Adamcik, S. Jordens and R. Mezzenga, *Biomacromolecules*, 2011, **12**, 1868–1875.
32 J. Adamcik, V. Castelletto, S. Bolisetty, I. W. Hamley and R. Mezzenga, *Angew. Chem., Int. Ed.*, 2011, **50**, 5495–5498.
33 I. A. Nyrkova, A. N. Semenov, A. Aggeli and N. Boden, *Eur. Phys. J. B*, 2000, **17**, 481–497.
34 A. Aggeli, I. A. Nyrkova, M. Bell, R. Harding, L. Carrick, T. C. B. McLeish, A. N. Semenov and N. Boden, *Proc. Natl. Acad. Sci. U. S. A.*, 2001, **98**, 11857–11862.
35 X. Periole, A. Rampioni, M. Vendruscolo and A. E. Mark, *J. Phys. Chem. B*, 2009, **113**, 1728–1737.
36 J. Adamcik and R. Mezzenga, *Macromolecules*, 2012, **45**, 1137–1150.

37 M. C. Phillips, *J. Lipid Res.*, 2013, **54**, 2034–2048.
38 T. Joy, J. Wang, A. Hahn and R. A. Hegele, *Clin. Biochem.*, 2003, **36**, 641–645.
39 W. C. Nichols, R. E. Gregg, H. B. Brewer and M. D. Benson, *Genomics*, 1990, **8**, 318–323.
40 J. O. Lagerstedt, G. Cavigiolio, L. M. Roberts, H. S. Hong, L. W. Jin, P. G. Fitzgerald, M. N. Oda and J. C. Voss, *Biochemistry*, 2007, **46**, 9693–9699.
41 M. Girych, G. Gorbenko, V. Trusova, E. Adachi, C. Mizuguchi, K. Nagao, H. Kawashima, K. Akaji, M. Phillips and H. Saito, *J. Struct. Biol.*, 2014, **185**, 116–124.
42 E. Adachi, H. Nakajima, C. Mizuguchi, P. Dhanasekaran, H. Kawashima, K. Nagao, K. Akaji, S. Lund-Katz, M. C. Phillips and H. Saito, *J. Biol. Chem.*, 2013, **288**, 2848–2856.
43 M. Groenning, *J. Chem. Biol.*, 2010, **3**, 1–18.
44 A. A. Bulychev, V. N. Verchoturov and B. A. Gulaev, *Current methods of biophysical studies*, Vyschaya shkola, Moscow, 1988.
45 J. R. Lakowicz, *Principles of fluorescent spectroscopy*, Springer, New York, 3rd edn, 2006.
46 Y. Domanov and G. Gorbenko, *Biophys. Chem.*, 2002, **99**, 143–154.
47 V. G. Ivkov and G. N. Berestovsky, *Dynamic structure of lipid bilayer*, Nauka, Moscow, 1981.
48 R. Dale, J. Eisinger and W. Blumberg, *Biophys. J.*, 1979, **26**, 161–194.
49 A. I. Sulatskaya, A. A. Maskevich, I. M. Kuznetsova, V. N. Uversky and K. K. Turoverov, *PLoS One*, 2010, **5**, e15385.
50 V. I. Stsiapura, A. A. Maskevich and I. M. Kuznetsova, *J. Phys. Chem. A*, 2007, **111**, 4829–4835.
51 A. Hawe, M. Sutter and W. Jiskoot, *Pharm. Res.*, 2008, **25**, 1487–1499.
52 A. D. Lúcio, C. C. Vequi-Suplicy, R. M. Fernandez and M. T. Lamy, *J. Fluoresc.*, 2010, **20**, 473–482.
53 S. A. Sanchez, M. A. Tricerri and E. Gratton, *Proc. Natl. Acad. Sci. U. S. A.*, 2012, **109**, 7314–7319.
54 T. Parasassi, E. K. Krasnowska, L. Bagatolli and E. Gratton, *J. Fluoresc.*, 1998, **8**, 365–373.
55 J. Adamcik and R. Mezzenga, *Curr. Opin. Colloid Interface Sci.*, 2012, **17**, 369–376.
56 O. Conchillo-Sole, N. S. de Groot, F. Avilés, J. Vendrell, X. Daura and S. Ventura, *BMC Bioinf.*, 2007, **8**, 65.
57 G. G. Tartaglia and M. Vendruscolo, *Chem. Soc. Rev.*, 2008, **37**, 1395–1401.
58 R. Linding, J. Schymkowitz, F. Rousseau, F. Diella and L. Serrano, *J. Mol. Biol.*, 2004, **342**, 345–353.
59 O. Gursky, X. Mei and D. Atkinson, *Biochemistry*, 2012, **51**, 10–18.
60 M. Das, X. Mei, S. Jayaraman, D. Atkinson and O. Gursky, *FEBS J.*, 2014, **281**, 2525–2542.
61 M. R. Krebs, E. H. Bromley and A. M. Donald, *J. Struct. Biol.*, 2005, **149**, 30–37.
62 C. L. Teoh, C. L. Pham, N. Todorova, A. Hung, C. N. Lincoln, E. Lees, Y. H. Lam, K. J. Binger, N. H. Thomson, S. E. Radford, T. A. Smith, S. A. Müller, A. Engel, M. D. Griffin, I. Yarovsky, P. R. Gooley and G. J. Howlett, *J. Mol. Biol.*, 2011, **4**, 1246–1266.
63 V. Trusova, G. Gorbenko, M. Girych, E. Adachi, C. Mizuguchi, R. Sood, P. Kinnunen and H. Saito, *J. Fluoresc.*, 2015, **25**, 253–261.
64 R. Gautier, D. Douguet, B. Antonny and G. Drin, *Bioinformatics*, 2008, **24**, 2101–2102.
65 R. Keller, *Int. J. Mol. Sci.*, 2011, **21**, 5577–5591.
66 V. Lulevich, C. C. Zimmer, H. S. Hong, L. W. Jin and G. Y. Liu, *Proc. Natl. Acad. Sci. U. S. A.*, 2010, **107**, 13872–13877.
67 A. W. P. Fitzpatrick, S. T. Park and A. H. Zewail, *Proc. Natl. Acad. Sci. U. S. A.*, 2013, **110**, 10976–10981.
68 J. J. Kremer, D. J. Sklansky and R. M. Murphy, *Biochemistry*, 2001, **40**, 8563–8571.
69 J. Nicolay, S. Gatz, G. Liebig, E. Gulbins and F. Lang, *Cell. Physiol. Biochem.*, 2007, **19**, 175–184.
70 A. Hirano, H. Yoshikawa, S. Matsushita, Y. Yamada and K. Shiraki, *Langmuir*, 2012, **28**, 3887–3895.
71 L. Milanesi, T. Sheynis, W. F. Xue, E. V. Orlova, A. L. Hellewell, R. Jelinek, E. W. Hewitt, S. E. Radford and H. R. Saibil, *Proc. Natl. Acad. Sci. U. S. A.*, 2012, **109**, 20455–20460.
72 D. A. Quint, A. Gopinathan and G. M. Grason, *Soft Matter*, 2012, **8**, 9460–9468.
73 J. Adamcik and R. Mezzenga, *Soft Matter*, 2011, **7**, 5437–5443.
74 D. Kurouski, W. Lauro and I. K. Lednev, *Chem. Commun.*, 2010, **46**, 4249–4251.

